PLEASE CITE THIS ARTICLE AS DOI: 10.1063/5.0021541

Towards an experimental proof of superhydrophobicity enhanced by quantum fluctuations freezing on a broadband-absorber metamaterial

Michaël Sarrazin,[1, a)] Ismaël Septembre,[2] Anthony Hendrickx,[2] Nicolas Reckinger,[2] Louis Dellieu,[2] Guillaume Fleury,[3] Christian Seassal,[4] Radoslaw Mazurczyk,[4] Sébastien Faniel,[5] Sabrina Devouge,[6] Michel Voué,[6] and Olivier Deparis[2, b)]

[1)] *Institut UTINAM, CNRS/INSU, UMR 6213, Université Bourgogne – Franche-Comté, 16 route de Gray, F-25030 Besançon Cedex, France*

[2)] *Department of Physics, University of Namur, 61 rue de Bruxelles, B-5000 Namur, Belgium*

[3)] *Univ. Bordeaux, CNRS, Bordeaux INP, LCPO, UMR 5629, F-33600, Pessac, France*

[4)] *Université de Lyon, Institut des Nanotechnologies de Lyon INL-UMR 5270, CNRS, Ecole Centrale de Lyon, 36 Avenue Guy de Collongue, F-69134 Ecully Cedex, France*

[5)] *Institute of Information and Communication Technologies, Electronics and Applied Mathematics, Université Catholique de Louvain, Place du Levant 3, B-1348 Louvain-la-Neuve, Belgium*

[6)] *Physics of Materials and Optics, Research Institute for Materials Science and Engineering, University of Mons, Mons B-7000, Belgium*

Previous theoretical works suggested that superhydrophobicity could be enhanced through partial inhibition of the quantum vacuum modes at the surface of a broadband-absorber metamaterial which acts in the extreme ultraviolet frequency domain. This effect would then compete with the classical Cassie-Baxter interpretation of superhydrophobicity. In this article, we first theoretically establish the expected phenomenological features related to such a kind of "quantum" superhydrophobicity. Then, relying on this theoretical framework, we experimentally study patterned silicon surfaces on which organosilane molecules were grafted, all the coated surfaces having similar characteristic pattern sizes but different profiles. Some of these surfaces can indeed freeze quantum photon modes while others cannot. While the latter ones allow hydrophobicity, only the former ones allow for superhydrophobicity. We believe these results lay the groundwork for further complete assessment of superhydrophobicity induced by quantum fluctuations freezing.

PACS numbers: 47.55.dr,61.30.Hn,68.90.+g

I. INTRODUCTION

A few years ago, it was shown, from first-principle numerical calculations, that superhydrophobicity of nanostructured surfaces is dramatically enhanced by tuning vacuum photon-modes via proper design of the surface corrugation, independently of any kind of chemical functionalization[1–3]. While nanostructures are commonly used for developing superhydrophobic surfaces, available wetting theoretical models ignore the effect of vacuum photon-modes alteration on van der Waals forces and thus on hydrophobicity[4–9]. Quantum physics teaches us that the van der Waals force results from the exchange of virtual photons – i.e. quantum vacuum fluctuations of the electromagnetic field – between both interacting bodies[10–14]. Then, considering nanostructured surfaces designed to form a thin metamaterial layer with ultra-broadband and wide-angle absorption of electromagnetic radiation, we could preclude the exchange of virtual photons thus inducing the collapse of the van der Waals force[1,2]. In this context, the study of non-wetting phenomena is a clever way to indirectly probe the van der Waals interactions and water obviously appears to be the most relevant liquid to study those effects. In spite of this exciting possibility, experimental investigations are still missing which would support such a quantum approach. In this article, we address this problem from a practical point of view and shed light on how freezing of electromagnetic quantum fluctuation allows a kind of superhydrophobicity and could be experimentally demonstrated. In section II, we recall the theoretical framework and provide a new practical description and context. In section III, we report on our first experimental attempts to observe the effect of quantum freezing on superhydrophobicity by studying the wettability of controllable nanostructured silicon coated with organosilane self-assembled monolayers. Our results suggest that superhydrophobicity shows up only in those samples for which freezing of quantum photon modes was predicted to take place. We believe these results make a significant case in the experimental proof of superhydrophobicity enhancement by freezing of electromagnetic quantum fluctuations.

[a)] Electronic mail: michael.sarrazin@ac-besancon.fr; Corresponding author

[b)] Electronic mail: olivier.deparis@unamur.be; Corresponding author

II. THEORETICAL FRAMEWORK

The main contributions to van der Waals interactions come from virtual photon exchange in the Extreme Ultra-Violet (EUV) domain[1–3,15,16]. As shown in our previous theoretical studies, an ultra-broadband and wide-angle electromagnetic absorber in EUV domain should then preclude relevant photon exchange between the absorber and a water droplet, thus inducing van der Waals interactions between them to collapse[1,2]. As the surface tension of the water droplet dominates – over its interaction with the broadband absorber surface – water cannot spread on it [1]. (see Fig. 1). As a result, an ultra-broadband and wide-angle absorber in the EUV domain should act as a superhydrophobic metamaterial. Such a broadband absorber metamaterial can be designed by decorating a flat substrate with conical nanostructures organized as a subwavelength periodical array[1,2]. This kind of nanostructured surface is known to act as an optically antireflecting layer as it is equivalent to a graded index multilayer[1,2]. Using a numerical code based on Rigourous Coupled Wave Analysis (RCWA)[17], it is possible to compute the scattering matrices (S matrices) describing light wave interactions with surfaces – nanostructured or not. A relevant expression of van der Waals forces connects these interactions to S matrices at a quantum level[1,2,18–21]. Between the interfaces separating two interacting bodies by a distance L, the potential energy $U(L)$ related to van der Waals forces is given by the well-known Hamaker expression[22]:

$$U(L) = -\frac{A_H}{12\pi L^2}, \tag{1}$$

where A_H is the Hamaker constant. A_H can be derived through heavy numerical computations of the scattering matrices describing the problem under study. In our previous numerical studies, we considered nanostructuring by an hexagonal array of cones as a theoretical framework. For this kind of nanostructured surface, the Hamaker constant was computed against the cone height h[1,2] leading to a dependence on h which is well fitted by:

$$A_H \sim A_{H,0}\frac{1}{1+h/h_0}, \tag{2}$$

with $h_0 \sim a_0/\pi$, where a_0 is the grating parameter – i.e. the spatial period of the cone array – and $A_{H,0}$ is the Hamaker constant of the flat surface ($h = 0$). Such a convenient expression can also be derived in the context of a simple analytical model introduced in this article, in order to clarify the physical meaning of Eq. 2 and to drive easily experimental investigation. For the sake of clarity, details of the following mathematical arguments are given in Appendices A and B.

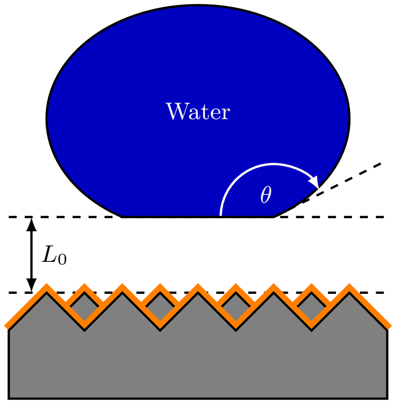

FIG. 1. (Color online). Sketch of the studied system. At equilibrium, the water droplet is separated from the nanostructured surface by the distance L_0[16]. The droplet presents a contact angle θ. The nanostructured silicon (grey) is coated (orange) with organic molecules in order to emulate a nanostructured molecular solid surface.

Let us consider media (bodies) 1 and 2 occupying the half-spaces $z < 0$ and $z > L$, respectively, and separated by a vacuum. At absolute zero temperature, it can be shown that the van der Waals interaction potential energy U is given by[18–21] $U = \sum_p \frac{1}{2}\hbar(\omega_p(L) - \omega_p(L \to \infty))$ where $\omega_p(L)$ is the eigen angular frequency – for a given polarization – of the pth vacuum photon-mode available between the two media facing each other. Using the Cauchy's argument principle and the analytical properties of the Fresnel coefficients of each body, the interaction energy is then given by the exact expression[19–21]:

$$U(L) = \frac{\hbar}{2\pi}\sum_{m=s,p}\int\frac{\mathrm{d}^2 k_{/\!/}}{(2\pi)^2}\int_0^\infty \mathrm{d}\xi \tag{3}$$
$$\times \ln(1 - R_1^m(i\xi,\mathbf{k}_{/\!/})R_2^m(i\xi,\mathbf{k}_{/\!/})e^{-2\kappa L}),$$

where $\kappa = \sqrt{\frac{\xi^2}{c^2} + \left|\mathbf{k}_{/\!/}\right|^2}$, ${R_1}^m$ (${R_2}^m$) is the complex reflection coefficient of slab 1 (slab 2) in the m polarization state (s or p states) and $k_{/\!/}$ is the parallel component of the photon wave vector. The use of the complex angular frequency $\omega = i\xi$ arises from numerical computation considerations. Although this theory has been derived at zero temperature, it must be noticed that Eq. 3 can be perfectly used at room temperature provided that $\hbar\omega_p \gg k_B T$, a condition that is satisfied for all photon

---

[1] Many liquids are often used to study wetting (or non-wetting) phenomena, such as diiodomethane, DMSO, ethanol, cyclohexane, or ethylene glycol. For a corrugated interface, the required condition to obtain enhanced non-wetting phenomena is that the contact angle on the flat interface on the same material is $\theta \geq 90°$, i.e. the flat surface is already non-wettable. This is necessary to obtain an almost flat liquid-solid interface as required for the Cassie-Baxter approach of the superhydrophobicity or for the present quantum model. From our own measurements on flat silicon grafted with organosilane molecules (the material used herein), none of the above mentioned liquids meet the expected condition. The best result was obtained for ethylene glycol with $\theta = 87.5 \pm 2.9°$ on flat grafted silicon. As a result, water is better than any other fluid for the present purpose.

energies involved here as shown elsewhere[1–3,15,16]. Such a condition means that the interaction reduces only to the effect of virtual photon exchange while the contribution of blackbody photons can be neglected. Independently of this consideration, the interaction energy given by Eq. 3 still exhibits a temperature dependence simply because the dielectric properties of materials – permittivity values involved in the reflection coefficients – are temperature dependent.

Let us take medium 1 as the solid and medium 2 as the liquid. Hereafter, we propose a useful phenomenological theoretical description of the superhydrophobicity tuning induced by the use of a slab of metamaterial having ultra-broadband and wide-angle absorption added on the flat interface of the medium 1 in order to form a corrugated interface. For convenience, the reflection coefficient R_c of the corrugated interface can be related to the reflection coefficient of the initially flat interface R_f, whatever the polarization state is, by using the ansatz:

$$R^m_{1,c} \to R^m_{1,f}\ \Lambda\left(\omega, h, a\right), \tag{4}$$

where $\Lambda\left(\omega, h, a\right)$ is a function of the incident wave angular frequency ω, of the metamaterial slab's geometry (layer thickness h) and its physical properties (effective absorption coefficient a, see below).

In the following, the metamaterial under interest is obtained from the flat interface by carving the surface of the solid across the depth h between 0 and 100 nm (or more), for instance, hence creating on the surface an array of nanospikes – roughly of conical or pyramidal shape – with a typical base about 10 nm and a high aspect-ratio[1,2]. The conical, or pyramidal, shape of these nanospikes provides a layer with an effective gradient index across the thickness h, acting as a antireflective layer such that the corrugated interface now exhibits an ultra-broadband and wide-angle absorption[1,2]. This effect is well-known, for instance, in black silicon where surface nanostructuring transforms a flat silicon wafer into a nearly perfect black material[23–26]. In this case, it is well-known that[23]:

$$\Lambda\left(\omega, h, a\right) = e^{-a(\omega/c)h}, \tag{5}$$

where a is an effective absorption coefficient here supposed to be constant against ω. Obviously, this equation corresponds to the Beer–Lambert law with $a = 2\mathtt{Im}\left\{n\right\} = 2n''$, which is applied to an interface covered by an idealized perfect absorbing layer with a thickness h and with an effective optical index n (see Appendix A for the derivation of n). Theoretically, this model is justified provided that the reflection of the absorbing layer is indeed negligible, i.e. if the highly antireflecting properties are allowed by an effective gradient index. Experimentally, this simple model is very well justified for black silicon[23–26] for instance.

From Eqs. 1, 3 and 4 it can be shown (see Appendix B for details) that the Hamaker constant can be recast as:

$$A_H = f\, A_{H,0}, \tag{6}$$

where $A_{H,0}$ is the Hamaker constant describing the interaction between the liquid and the flat interface, i.e. without the metamaterial slab, and f is a function which describes the effect of the metamaterial. For a metamaterial layer made of the array of cones described above *via* Eq. 5, we obtain (see Appendix B):

$$f = \frac{1}{1 + h/h_0} \tag{7}$$

It should be noted that, for an array of cylinders, f is a constant which does not depend on the metamaterial layer thickness h[1,3]. As justified later herein, this makes cylinder-based metamaterials irrelevant to demonstrate quantum effect on hydrophobicity[1,3].

The above derivation of the Hamaker constant is motivated by our will to compare theoretical predictions with experiments. It is well-known that Hamaker's theory is able to predict the equilibrium contact angle of liquid droplets on a surface[11], in general, and of water droplets in particular[13]. Indeed, from the van der Waals potential energy calculated between a solid and a liquid, we can immediately deduce[13] the corresponding contact angle θ:

$$\cos(\theta) = -1 + \frac{|U(L_0)|}{\gamma_l}, \tag{8}$$

where $U(L_0)$ is the potential energy between the two media separated by the distance L_0, which is the equilibrium separation distance[16] between the water droplet and the surface. This distance, originally defined for a flat surface[16], remains about the same when the solid surface is corrugated as shown elsewhere[13]. In Eq. 8, γ_l is the liquid surface tension.

As a result, from Eqs. 1, 6, and 8, the contact angle associated with the nanostructured surface can be easily expressed through the relation:

$$\cos(\theta) = -1 + (1 + \cos(\theta_0))\, f \tag{9}$$

which results from the quantum electrodynamics interpretation of the van der Waals interfacial forces and where θ_0 is the contact angle on the flat surface. For the cone array slab, using Eq. 7, one gets:

$$\cos(\theta) = -1 + (1 + \cos(\theta_0))\,\frac{1}{1 + h/h_0}, \tag{10}$$

By setting $h = 0$ in Eq. 10, one recovers the contact angle associated with the corresponding flat surface.

Nevertheless, it could be suggested that Eq. 10 could be also interpreted through the usual Cassie-Baxter

PLEASE CITE THIS ARTICLE AS DOI: 10.1063/5.0021541

model[4], which originates from a pure thermodynamic and geometrical analysis. We now underline that such an alternative interpretation is not valid. Let us start with the Cassie-Baxter expression[4]:

$$\cos(\theta) = f_1 \cos\theta_1 + f_2 \cos\theta_2, \tag{11}$$

with $f_1 + f_2 = 1$, and where f_1 and f_2 are the fractional areas of media composing the nanostructured surface, here respectively the air and the substrate. Hence, θ_1 would be the contact angle with the air, i.e. $\theta_1 = 180°$, and θ_2 would be the contact angle with the flat substrate, i.e. $\theta_2 = \theta_0$. By assuming Eq. 11 to be equivalent to Eq. 10, we would get for f_2 (and $f_1 = 1 - f_2$):

$$f_2 = \frac{1}{1 + h/h_0}. \tag{12}$$

On the other hand, according to the Cassie-Baxter approach, f_2 is the fractional area of liquid in contact with the surface S_2 of the substrate material. By noting S_1 the area of the liquid/air interface, it comes:

$$f_2 = \frac{S_2}{S_1 + S_2} = \frac{1}{1 + S_1/S_2}. \tag{13}$$

Considering Eqs. B14 and 12, Eq. 13 could be interpreted in the context of the Cassie-Baxter approach if and only if:

$$\frac{S_1}{S_2} = \frac{\pi h}{a_0}. \tag{14}$$

However, even when neglecting air pressure and liquid weight, S_1 and S_2 must depend on the exact geometry of the nanostructure (spikes), on the deformation of the liquid-air interface due to surface tension, and on the extend of the wet surface at the top of the spikes. In our quantum mechanically derived model, the ratio only depends on the height of the spikes (not on their actual geometry) and on the lattice parameter of the array of these spikes. As a matter of fact, there is no trivial geometrical construction that allows us to accept such an identity (Eq. 14), except by pure coincidence. For this reason, the main outcome of our model, i.e. Eq. 10, cannot be interpreted according to the Cassie-Baxter model. From a fundamental point of view, Eq. 10 results from optically-controlled suppression of vacuum photon modes responsible for van der Waals interaction. As a consequence, any experimental evidences of a wetting behaviour following Eq. 10 would be a signature of a superhydrophobic effect induced by optically-controlled suppression of vacuum photon modes. The next section reports on our very first attempts to check this statement experimentally.

Before reporting and discussing results, we point out that, for a cylinder-based metamaterial slab, as f is constant, it is always possible to relate f to geometrical parameters, by resorting solely to a Cassie-Baxter model, for instance. For example, considering an hexagonal array of cylinders with radius r_0, one gets $f = (2\pi/\sqrt{3})(r_0/a_0)^2$. Unfortunately, in this case and as shown elsewhere[1,3], *ab initio* numerical computations based on the quantum derivation of the van der Waals forces do not allow us to discriminate between quantum contributions and thermodynamical ones in a Cassie-Baxter approach. This is further discussed in the next section.

III. EXPERIMENTAL RESULTS

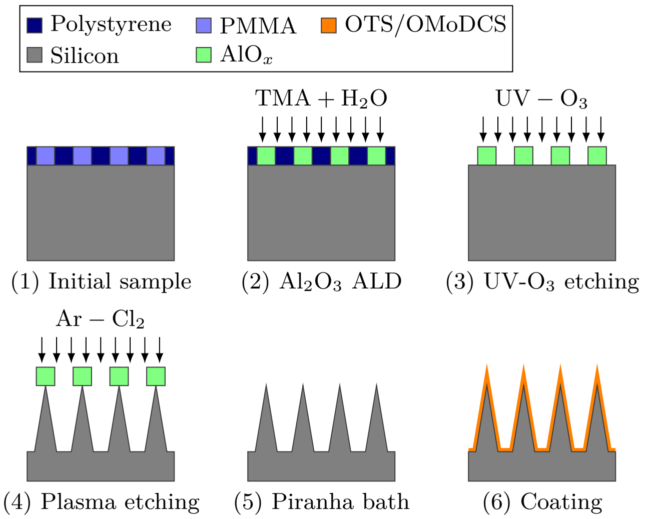

FIG. 2. (Color online). Sketch of each fabrication step 1 to 6 detailed in the text. 1. Formation of honeycomb structure of PMMA self-assembled studs in a PS matrix using block copolymer nano-manufacturing. 2. PMMA domain conversion into Al$_x$O$_y$ (green) by sequential infiltration synthesis. 3. Selective removal of the PS matrix using UV-O$_3$ treatment. 4. Silicon etching by RIE with Al$_x$O$_y$ nanostructures as hard mask. 5. Hard mask stripping. 6. Organosilane monolayer grafting.

As an experimental platform to check our theoretical predictions, nanopatterned silicon samples were fabricated using block copolymer nano-manufacturing and coated with two kinds of organosilane monolayers: octadecyltrichlorosilane (OTS) or octadecylmethoxydichlorosilane (OMoDCS). These molecules bear the same aliphatic chain ($n = 18$) and only differ due to the substitution of a methoxy group (OMoDCS) instead of a chloride (OTS) on the silicon atom. This substitution allows an easier control of the surface grafting. Such a coating was motivated by our previous theoretical works[1,2] where nanopatterned surfaces of molecular materials – such as polyethylene – where considered. This avoided some difficulties to construe van der Waals interactions with covalent materials. In the present work, silicon facilitates manufacturing at the nanometer scale, but the organic coating allows to keep the choice of molecular

Sample	h (nm)	a_0 (nm)	r_0 (nm)	Graft	θ (°)
C35-5'	200 ± 5	35 ± 2	15 ± 2	OTS	159 ± 3
C35-3'	120 ± 5	35 ± 2	15 ± 2	OMoDCS	130 ± 3
C23-5'	100 ± 5	23 ± 2	10 ± 2	OMoDCS	161 ± 3
C23-3'	85 ± 5	23 ± 2	8.5 ± 2	OMoDCS	142 ± 3

TABLE I. Samples used for wetting characterization (Cxx-y' with xx the lattice parameter in nm and y the etching time in min). h: structure's height, a_0: lattice parameter, r_0: structure's radius on surface, Graft: Organosilane monolayer, θ: equilibrium contact angle.

materials as a working hypothesis[2].

The samples exhibit roughly hexagonal arrays of nanopillars or nanospikes. In order to fabricate our samples, we followed a protocol inspired by the work of Checco *et al*[28,29] and we adapted it in order to reach smaller lateral features (i.e. lattice parameter a_0) that are mandatory for the problem under consideration. This constraint set a huge challenge for experimentalists since we had to create spikes as close as a few tens of nanometers to one another and as high as one hundred nanometers.

We proceeded as follows (steps 1-3: formation of a nanopatterned mask on silicon, steps 4-5: etching of silicon through the mask, steps 6: conformal grafting of an organic monolayer on the nanostructured silicon surface, see Fig. 2):

1. Silicon wafers were spin-coated with a poly(styrene)-b-poly(methyl methacrylate) (PS-b-PMMA) block copolymer solution on a silicon substrate grafted with a neutral statistical (PS-stat-PMMA) copolymer, and thermally annealed, resulting in the formation of an honeycomb structure of PMMA self-assembled studs in a PS matrix.

2. The PMMA core was substituted by aluminium oxide (Al_xO_y) by sequential infiltration synthesis performed within an Atomic Layer Deposition (ALD) apparatus using trimethylaluminum (TMA) and H_2O as precursors.

3. The PS matrix was removed by UV-O_3 treatment.

4. Silicon was etched by RIE (Reactive Ion Etching with Ar and Cl_2 plasma in ratio 4:1) with the Al_xO_y nanostructures as a hard mask.

5. The hard mask was removed in a bath of "piranha" solution (H_2O_2 + H_2SO_4 in ratio 3:1).

6. Etched silicon surfaces were grafted with an organic layer of OTS or OMoDCS (Degreasing: 10 min ultrasonication (US) in acetone + 10 min US in methanol. Activation: 30 min in H_2SO_4/H_2O_2 (70:30) solution at 90 °C. Grafting solutions: 4 mM OTS in hexane (0 °C, 60 min) or 2 mM OMoDCS in hexane (RT, 120 min). Rinsing: 2 × 5 min US in $CHCl_3$).

Two different PS-b-PMMA block copolymers with different intrinsic periodicity (i.e., C23 and C35 with cylinder-to-cylinder distance of 23 and 35 nm, respectively) were used to fabricate the corrugated patterns in order to obtain different lattice parameters. In total, 17 samples have been realized, but only 4 samples had the appropriate geometry for testing our prediction after steps 2 to 5 (silicon etching and mask removal). This means that the manufacturing process provides – with a success rate of 24% – the samples with the expected lateral corrugation distance, with a weak dispersion, and with patterns sufficiently similar to each other. These samples were then grafted with organic molecules in order to emulate the nanostructured molecular solid surface previously considered in our *ab initio* theoretical model[1]. Hence, the initial nanostructured silicon wafer served only as a mechanical support for the organic monolayer.

The properties of these samples are summarized in Table 1 and their typical surface pattern are shown in Fig. 3 by scanning electron microscopy (SEM). Equilibrium contact angle measurements were performed on these samples and the corresponding results are reported in Table 1. The measured angle values and their uncertainties are also shown in Fig. 4 (blue bars). For the flat surfaces, organosilane layer thickness determined by spectroscopic ellipsometry after optimisation of the grafting process were in agreement with the literature values (OTS: 3.0 ± 0.8 nm and OMoDCS: 2.3 ± 0.3 nm). For the same surface, the advancing contact angles were $109 \pm 1°$ (OTS) and $110 \pm 1°$ (OMoDCS). Nanostructuration clearly induces an increase of the advancing contact angles. On the basis of usually accepted criteria for superhydrophobicity (contact angle larger than 150° and low contact angle hysteresis), samples C35-5' and C23-5', respectively corresponding to the cones and spikes nanostructures, can be considered as superhydrophobic.

---

[2] It can be proved that just few nanometers of coating material allows to erase the effects of the covered medium[3,16].

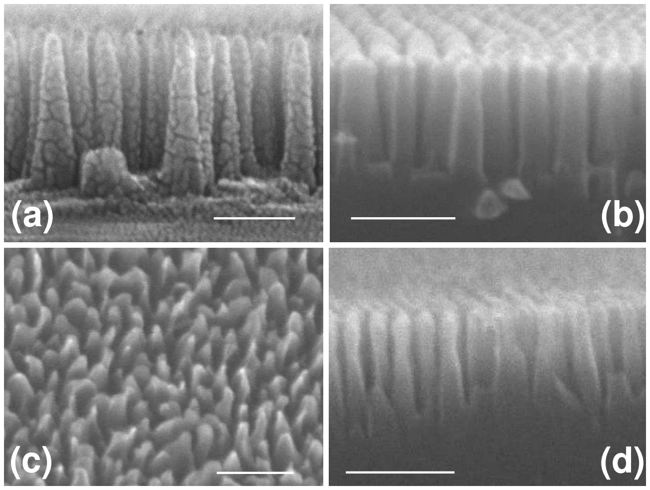

FIG. 3. Scanning electron microscopy images of nanopatterned silicon surfaces for C35-5' sample (a), C35-3' sample (b), C23-5' sample (c) and C23-3' sample (d). Scale bar: 100 nm.

Using Eq. 10, we computed the theoretical contact angles using the reported experimental flat surface contact angle, as well as the height h and the periodicity a_0 of the nanostructures which were estimated from SEM observations. The observed nanostructures were classified according to two extreme shapes, namely cylindrical pillars and sharp cones (spikes). The results are reported in Fig. 4 (red bars) together with uncertainties resulting from error propagation of the experimental inputs. As expected from our theoretical analysis, since pillar-like nanostructures offer no significant anti-reflecting properties in UV domain[1–3] (due to the absence of effective index gradient), Eq. 10 cannot be applied to C35-3' and C23-3' nanostructures, which explains the differences between theoretical and measured angles. By contrast, Eq. 10 should be highly relevant to spikes (samples C35-5' and C23-5') since they allow for the graded-index profile at the origin of the optically-controlled suppression of vacuum photon modes. Indeed, one can observe that experimental and theoretical contact angles match very well in both C35-5' an C23-5' samples (see Fig. 4). However, it is worth noticing that general and complex exact numerical computations using Eq. 3 for cylindrical pillars – previously achieved for polyethylene[3] – led to a contact angle about 140° similar to those of samples C35-3' and C23-3', thus strengthening our approach derived from Eq. 3. Nevertheless, as explained in the previous section, the theoretical behaviour of the hydrophobic properties of the cylindrical-based effective layer given by Eq. 9 (f being constant against h) can be also discussed, for instance, on the basis of the Cassie-Baxter approach (with $f = (2\pi/\sqrt{3})(r_0/a_0)^2$). Then, using values of r_0 and a_0 given in Table 1, Eq. 9 leads to the following contact angles: $124 \pm 9°$ (C35-3') and $132 \pm 13°$ (C23-3'). Despite large uncertainties, these predicted values are compatible with the measured contact angles. In conclusion, not only the cylindrical pillars do not enable to obtain superhydrophobicity, but they do not allow us to discriminate between classical effects and quantum ones.

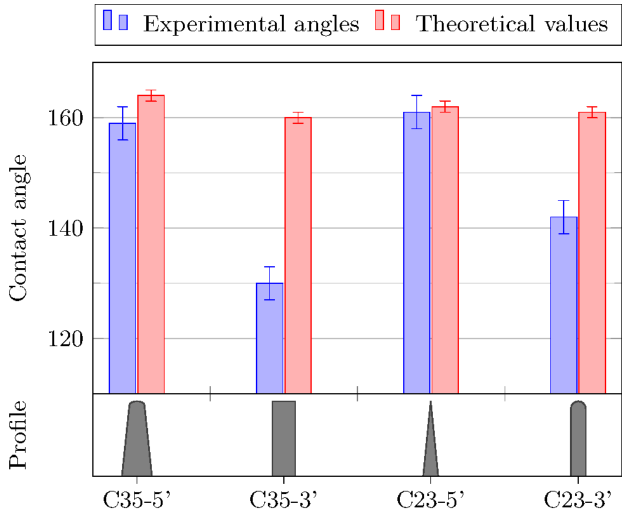

FIG. 4. (Color online). Comparison for each kind of patterns between experimental (blue) contact angles (in degrees) and theoretical ones (red) from Eq. 10 assuming quantum contributions inducing superhydrophobicity. The patterns are classified according to two extreme shapes, i.e. pillars (cylinders) and spikes (sharp cones).

It could be then suggested that the present results – regarding surfaces covered with cones and spikes – could be also interpreted through a classical Cassie-Baxter model. For instance, instead of perfect cones, and as it could be suggested by SEM images, one could consider truncated cones surmounted by hemispheres with radius r_{top}. In such a case, the contact angle is given by the well-known relation[30]:

$$\cos\theta = n\pi r_{top}^2 (1 + \cos\theta_0)^2 - 1, \tag{15}$$

where n is the number of hemispheres per unit area for a hexagonal array, i.e. $n = 2/(a_0^2\sqrt{3})$. However, fitting r_{top} in order to match experimental data leads then to hemispheres' radii two times larger than those expected from SEM measurements. This discrepancy clearly invalidates such a Cassie-Baxter approach. It could also be objected that more complex classical models, for instance using finite element methods relying on Navier-Stokes equations[31–33], could maybe explain also these results. Nevertheless, the experimental study of wetting models on corrugated surfaces with lateral corrugations as close as 10 nm is complicated by complex manufacturing processes – hard to replicate – and by huge uncertainties on contact angle measurements[34,35]. This leaves us with a narrow experimental window in order to definitively validate or invalidate our model. Moreover, as shown by Eq. 15 for instance, superhydrophobic behaviour mainly depends on the geometrical properties of the top of the nanostructures in the Cassie-Baxter approach, while the quantum description given by Eq. 10

underlines the importance of the nanostructures' height. As a consequence, any remaining doubts on the exact mechanisms at play will only be resolved if one is able to improve the reliable production of a large number of samples with different profiles in order to increase the significance of the present experimental results and to be able to compare the classical and quantum models, for instance by looking for a dependance of the contact angle on the nanostructures' height. We hope that the present study will stimulate further research in this direction.

IV. CONCLUSIONS AND PERSPECTIVES

Previous theoretical works suggested that, superhydrophobicity can be induced through the use of a nanostructured surface that is designed to form a thin metamaterial layer with ultra-broadband and wide-angle absorption. This layer precludes the exchange of virtual photons and induces the collapse of the van der Waals force allowing to reach superhydrophobicity. We have given an interpretation of this fundamental concept through a phenomenological approach which allowed us to derive a simple effective contact angle formula that is the typical signature induced by quantum effects on superhydrophobicity. Using advanced masking and etching techniques for silicon wafer texturing at the nanometer scale and subsequent grafting of organic monolayers, we have realized unique deeply nanostructured surfaces covered by arrays of nanospikes or nanopillars in order to provide a plateform for assessing our model. In samples exhibiting nanospikes, we have measured static contact angles which could be interpreted as a result of the suppression of quantum fluctuations as predicted by our model. Further similar experiments will be considered in a next work in order to reinforce the first assessment of the model provided by these preliminary results.

ACKNOWLEDGMENTS

The authors thank Alexandre Felten and Francesca Cecchet for useful discussions and reading of the manuscript. This research used resources of the Electron Microscopy Service located at the University of Namur. This Service is member of the "Plateforme Technologique Morphologie – Imagerie" (MORPH-IM). G.F. gratefully acknowledges Arkema for providing the materials to prepare the block copolymer mask.

DATA AVAILABILITY

The data that support the findings of this study are available from the corresponding authors upon reasonable request.

Appendix A: Metamaterial effective optical index

When the surface is corrugated by an array of conical pillars, two effects occur: diffraction modes arising from the periodic lateral corrugation and refractive index gradient arising from the vertically aligned cones.

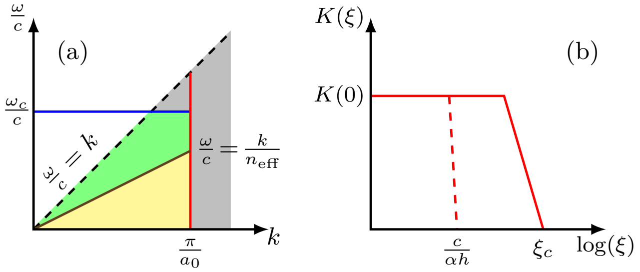

FIG. 5. (Color online). (a) Virtual photon dispersion between interfaces (grey) with frequency cut-off (permittivity cut-off) and wavevector cut-off (due to periodic array). Green and orange areas are equal and define the average dispersion relation and then the effective index n_{eff}. (b) The $K(\xi)$ function, Eq. B9, presents a typical low-band pass behaviour with a cut-off frequency at ξ_c, which is illustrated here. The dashed line illustrates the cut-off that is introduced in the Hamaker constant expression, Eq. B10, by the factor $e^{-\alpha(\xi/c)h}$.

First, in the long wavelength limit, a grating effective index n_{eff} can be defined, which is related to the wavevector cut-off effect due to the lateral corrugation characterized through the period a_0. Let us now estimate n_{eff}. As the medium is constituted by a set of periodic nanospikes with a period a_0, and since one deals with wavelengths greater than a_0, all diffraction orders of the periodically structured surface (i.e. grating) are evanescent except for the zeroth-order of diffraction (specular reflection). As a result, the electromagnetic field can efficiently penetrate the medium while being exponentially damped, allowing for a strong effective absorption of light. Since the surface has discrete translational symmetry in lateral directions (cf. periodical array), $k_{/\!/}$ should present a cut-off typically near π/a_0 at the border of the Brillouin zone. In addition, ω, and thus ξ, should present a typical cut-off $\xi_c \sim \omega_c$ beyond which the permittivity of the material tends to the vacuum permittivity. This consideration is general and valid for any material, as the frequency tends to infinity. In practice ω_c can be considered as finite. In addition, for short distances between interacting bodies, evanescent waves ($\frac{\omega^2}{c^2}n_{\mathrm{eff}}^2 - \left|\mathbf{k}_{/\!/}\right|^2 < 0$) dominate and must follow the dispersion relation $\frac{\omega}{c} < k_{/\!/}/n_{\mathrm{eff}}$. As a result, possible virtual photons parameters $(\omega, k_{/\!/})$ occupy the domains in $(\omega, k_{/\!/})$-space that are depicted in green and orange in Fig. 5a. Considering both wavevector and frequency finite limits, we decide to describe n_{eff} as the effective index which corresponds to the average dispersion relation separating green and orange domains into two equal parts. Then, from geometrical considerations, one easily shows that:

$$n_{\text{eff}} = \frac{2x^2}{2x-1} \text{ with } x = \frac{\pi c}{a_0 \xi_c}. \tag{A1}$$

In the following, we will assume that ξ_c is small enough compared to $\pi c/a_0$ so that[3] $n_{\text{eff}} \sim x$. In practice, x is of the order of ten.

Next, always in the long wavelength limit, the profile of the corrugation can lead to a refractive index gradient[1,2] $n_g(z)$ while z varies between the substrate ($z = 0$) and the top of the corrugation ($z = h$) in vacuum. For instance – for a cone array along an hexagonal lattice – one gets[1]:

$$n_g(z) = \sqrt{1 + \gamma(n_{\text{eff}}^2 - 1)(z-h)^2/h^2}, \tag{A2}$$

where $\gamma = \pi/(2\sqrt{3})$ is the 2D filling rate of the close-packed hexagonal lattice at the bottom of the cone ($z = 0$). For cylindrical pillars, on the other hand, it is worth noting that such a gradient does not exist but also that Eq. 5 cannot be applied as explained above (end of section A). In the present phenomenological approach, we replace $n_g(z)$ by a spatially averaged index which must correspond to the above mentioned effective optical index n of the absorbing layer. To derive such a mean index, one considers the optical path $\mathcal{L}$ through the absorbing layer of thickness h such as:

$$\mathcal{L} = \int_0^h n_g(z)\mathrm{d}z = nh, \tag{A3}$$

with

$$n = \frac{1}{h}\int_0^h n_g(z)\mathrm{d}z. \tag{A4}$$

It can be shown that[4]

$$n \sim (1/2)\, n_{\text{eff}}. \tag{A5}$$

Considering Eq. A5, we are able to find the searched expression for α:

$$\begin{aligned} \alpha = 2n &\sim n_{\text{eff}} \sim x \\ &\sim \frac{\pi c}{a_0 \xi_c}. \end{aligned} \tag{A6}$$

Appendix B: Hamaker constant derivation

In the case where the surface of body 1 is corrugated the expression of the potential energy, Eq. 3, becomes, thanks to Eq. 4 (the subscripts on the reflection coefficients in Eq. 4 are dropped for conciseness):

$$\begin{aligned} U(L) = \frac{\hbar}{2\pi} \sum_{m=s,p} \int \frac{\mathrm{d}^2 k_{/\!/}}{(2\pi)^2} \int_0^\infty \mathrm{d}\xi \\ \times \ln(1 - R_1^m(i\xi, \mathbf{k}_{/\!/})\Lambda\,(i\xi, h, \alpha)\, R_2^m(i\xi, \mathbf{k}_{/\!/}) e^{-2\kappa L}), \end{aligned} \tag{B1}$$

Considering Eq. 5 where a is now substituted by[5] $\alpha = 2n(i\xi)$, where we further assume that $n(i\xi) \sim n$ is constant, i.e. frequency-independent on the domain of interest. A tricky part of the present phenomenological approach lies in the estimation of the effective optical index n of the metamaterial layer, which is detailed in Appendix A.

Let us first rewrite Eq. B1 as:

$$\begin{aligned} U(L) = \frac{\hbar}{4\pi^2 L^2} \sum_{m=s,p} \int_0^\infty q\mathrm{d}q \int_0^\infty \mathrm{d}\xi \\ \times \ln(1 - R_1^m(i\xi, q/L)\Lambda\,(i\xi, h, \alpha)\, R_2^m(i\xi, q/L) e^{-2\rho}), \end{aligned} \tag{B2}$$

where we used: $(1/(2\pi)^2)\int \mathrm{d}^2 k_{/\!/} = (1/2\pi)\int k_{/\!/}\mathrm{d}k_{/\!/}$, and $\rho = \sqrt{\frac{\xi^2}{c^2}L^2 + q^2}$, with $q = k_{/\!/}L$. Using Eq. 1, the effective Hamaker constant A_H is directly deduced from Eq. B2:

$$\begin{aligned} A_H = -\frac{3\hbar}{\pi} \sum_{m=s,p} \int_0^\infty q\mathrm{d}q \int_0^\infty \mathrm{d}\xi \\ \times \ln(1 - R_1^m(i\xi, q/L)\Lambda\,(i\xi, h, \alpha)\, R_2^m(i\xi, q/L) e^{-2\rho}). \end{aligned} \tag{B3}$$

Recalling the expressions of the Fresnel coefficients for flat interfaces:

$$R_{1(2)}^s(\omega, k_{/\!/}) = \frac{k_{z,3} - k_{z,1(2)}}{k_{z,3} + k_{z,1(2)}}, \tag{B4}$$

$$R_{1(2)}^p(\omega, k_{/\!/}) = \frac{\varepsilon_3 k_{z,1(2)} - k_{z,3}\varepsilon_{1(2)}}{\varepsilon_3 k_{z,1(2)} + k_{z,3}\varepsilon_{1(2)}}, \tag{B5}$$

where $k_{z,i} = \sqrt{\frac{\omega^2}{c^2}\varepsilon_i - k_{/\!/}^2}$, we get, since $k_{/\!/} = q/L$:

$$\lim_{L\to 0} R_{1(2)}^s(i\xi, q/L) = 0, \tag{B6}$$

and

$$\lim_{L\to 0} R_{1(2)}^p(i\xi, q/L) = \frac{\varepsilon_3(i\xi) - \varepsilon_{1(2)}(i\xi)}{\varepsilon_3(i\xi) + \varepsilon_{1(2)}(i\xi)}. \tag{B7}$$

---

[3] $a_0 \approx 10$ nm, i.e. $\pi c/a_0 \approx 10^{17}$ rad·s^{-1}, while typical permittivity cut-off is about[27] 10^{16} rad·s^{-1}. Therefore x is of the order of 10 and the assumption $x \gg 1$ made to approximate n_{eff} by x from Eq. A1 is fully justified.

[4] Using the expression of Eq. A2 in Eq. A4, and setting $u = 1 - z/h$ and $p^2 = \gamma(n_{\text{eff}}^2 - 1)$, one gets $n = \int_0^1 \sqrt{1 + p^2u^2}\mathrm{d}u = \frac{1}{2}\left(\sqrt{1+p^2} + \arg\sinh(p)/p\right)$. For p great enough, $n \sim p/2$, and thus, for n_{eff} great enough – in the present context $n_{\text{eff}} \approx 5$ fulfilling the condition – $n \sim (\sqrt{\gamma}/2)n_{\text{eff}} \approx (1/2)\, n_{\text{eff}}$.

[5] Indeed, as $\exp(-a_\omega(\omega/c)h) = \exp(-2(\omega/c)\mathrm{Im}\,\{n(\omega)\}\,h) = \mathrm{Re}\,\{\exp(i2(\omega/c)n(\omega)h)\}$, then $\exp(-a_{i\xi}(i\xi/c)h) = \mathrm{Re}\,\{\exp(i2(i\xi/c)n(i\xi)h)\} = \exp(-2(\xi/c)n(i\xi)h)$ since $n(i\xi)$ is real.

Then, in the limit where L tends to zero:

$$A_H = -\frac{3\hbar}{\pi}\int_0^\infty q\mathrm{d}q\int_0^\infty \mathrm{d}\xi \times \ln(1-K(\xi)e^{-2q}\Lambda\left(i\xi,h,\alpha\right)), \tag{B8}$$

with

$$K(\xi) = \frac{\varepsilon_3(i\xi)-\varepsilon_1(i\xi)}{\varepsilon_3(i\xi)+\varepsilon_1(i\xi)}\frac{\varepsilon_3(i\xi)-\varepsilon_2(i\xi)}{\varepsilon_3(i\xi)+\varepsilon_2(i\xi)}. \tag{B9}$$

For most of usual materials, it can be verified that $K(\xi)$ is small enough such that $\ln(1-K(\xi)e^{-2q}\Lambda\left(i\xi,h,\alpha\right)) \sim -K(\xi)e^{-2q}\Lambda\left(i\xi,h,\alpha\right)$. In that case, the integral over q can be solved analytically, so that Eq. B8 becomes:

$$\begin{aligned} A_H &\sim \frac{3\hbar}{\pi}\int_0^\infty q\mathrm{d}q\int_0^\infty \mathrm{d}\xi K(\xi)e^{-2q}\Lambda\left(i\xi,h,\alpha\right) \\ &= \frac{3\hbar}{4\pi}\int_0^\infty \mathrm{d}\xi K(\xi)\Lambda\left(i\xi,h,\alpha\right). \end{aligned} \tag{B10}$$

For a flat interface (i.e. $h=0$, for instance), Eq. B10 reduces to:

$$\begin{aligned} A_{H,0} &= \frac{3\hbar}{4\pi}\int_0^\infty \mathrm{d}\xi K(\xi) \\ &= \frac{3\hbar}{4\pi}\int_0^\infty \mathrm{d}\xi \\ &\quad\times\frac{\varepsilon_3(i\xi)-\varepsilon_1(i\xi)}{\varepsilon_3(i\xi)+\varepsilon_1(i\xi)}\frac{\varepsilon_3(i\xi)-\varepsilon_2(i\xi)}{\varepsilon_3(i\xi)+\varepsilon_2(i\xi)}, \end{aligned} \tag{B11}$$

which is the well-known expression of the Hamaker constant at absolute zero temperature albeit valid up to the room temperature[3,16].

On the other hand, using Lorentz description[27] of the dielectric functions $\varepsilon(i\xi)$ and using the expression for $K(\xi)$ (see Eq. B9), one can verify that $K(\xi)$ possesses globally a low-pass spectral behaviour shown in Fig. 5b. As $K(\xi)$ is almost constant until the cut-off is reached at ξ_c, one can approximate $A_{H,0}$ by:

$$\begin{aligned} A_{H,0} &\sim \frac{3\hbar}{4\pi}K(0)\xi_c \\ &\sim \frac{3\hbar}{4\pi}\frac{\varepsilon_3(0)-\varepsilon_1(0)}{\varepsilon_3(0)+\varepsilon_1(0)}\frac{\varepsilon_3(0)-\varepsilon_2(0)}{\varepsilon_3(0)+\varepsilon_2(0)}\xi_c. \end{aligned} \tag{B12}$$

Now, in Eq. B10, that is for a nanostructured interface, the factor $\Lambda\left(i\xi,h,\alpha\right)=e^{-\alpha(\xi/c)h}$ (from Eq. 5) introduces a new cut-off frequency at $c/\alpha h$, which depends on h. A careful analysis shows that[6]:

$$A_H \sim A_{H,0}\frac{1}{1+h/h_0}, \tag{B13}$$

with $h_0 = c/(\xi_c\alpha)$. Using the approximation of Eq. A6 which relates α to a_0 and ξ_c, we get:

$$h_0 = \frac{a_0}{\pi}. \tag{B14}$$

Then, Eqs. B13 is the searched expression, Eq. 2, giving the dependence of Hamaker constant against the cone height h, *i.e.* the thickness h of the effective broadband absorber metamaterial under consideration.

REFERENCES

[1] L. Dellieu, O. Deparis, J. Muller, M. Sarrazin, Phys. Rev. Lett. **114**, 024501 (2015).

[2] L. Dellieu, O. Deparis, J. Muller, B. Kolaric, M. Sarrazin, Phys. Rev. B **92**, 235418 (2015).

[3] L. Dellieu, *Electrodynamical approach of surface multifunctionality: the tuning of the Lifshitz-van der Waals interactions*, Ph.D. Thesis, University of Namur, Belgium, 2016.

[4] A.B.D Cassie and S. Baxter, Trans. Faraday Soc., **40**, 546 (1944).

[5] C. Cuvelier, A. Segal, and A. A. van Steenhoven, *Finite Element Methods and Navier-Stokes Equations*, Springer Science & Business Media, 1986.

[6] K. L. Mittal, *Advances in Contact Angle, Wettability and Adhesion*, John Wiley & Sons, 2013.

[7] X. Yao, Y. Hu, A. Grinthal, T.-S. Wong, L. Mahadevan, and J. Aizenberg, Nat. Mater. **12**, 529 (2013).

[8] J. De Coninck and T. D. Blake, Ann. Rev. Mater. Res. **38**, 1 (2008).

[9] C. Yang, U. Tartaglino, and B. N. J. Persson, Phys. Rev. Lett. **97**, 116103 (2006).

[10] J.D. van der Waals, *Over de Continuiteit van den Gas- en Vloeistoftoestand*, Ph.D. Thesis, Leiden University, 1873.

[11] D.B. Hough, L.R. White, Adv. Colloid Interface Sci. **14**, 3 (1980).

[12] W. Fenzl, Ber. Bunsenges. Phys. Chem **98**, 389 (1994).

[13] C. J. Drummond and D. Y. C. Chan, Langmuir **13**, 3890 (1997).

[14] W. Fenzl, Europhys. Lett. **64**, 64 (2003).

[15] J. Mahanty, B.W. Ninham, *Dispersion Forces*, Academic Press London, 1976.

[16] J. Israelachvili, *Intermolecular and surface forces*, Academic Press Elsevier, 2011.

[17] M. Sarrazin, J.-P. Vigneron, and J.-M. Vigoureux, Phys. Rev. B **67**, 085415 (2003).

[18] E. M. Lifshitz, Sov. Phys. JETP **2**, 73 (1956).

[19] F. S. S. Rosa, D. A. R. Dalvit, and P. W. Milonni, Phys. Rev. Lett. **100**, 183602 (2008).

[20] A. Lambrecht, P. A. M. Neto, and S. Reynaud, New J. Phys. **8**, 243 (2006).

[21] R. Messina and M. Antezza, Phys. Rev. A **84**, 042102 (2011).

[22] Hamaker, H. C. Physica **4**, 1058 (1937).

[23] H. M. Branz, V. E. Yost, S. Ward, K. M. Jones, B. To, P. Stradins, APL **94**, 231121 (2009).

[24] S. Koynov, M. S. Brandt, M. Stutzmann, APL **88**, 203107 (2006).

[25] S. Ma , S. Liu, Q. Xu, J. Xu, R. Lu, Y. Liu, Z. Zhong, AIP Adv. **8**, 035010 (2018).

[26] C.-H. Hsu, J.-R. Wu, Y.-T. Lu, D. J. Flood, A. R. Barron, L.-C. Chen, Mat. Sci. Semicon. Proc. **25**, 2 (2014).

[27] V. A. Parsegian and G. H. Weiss, J. Colloid Interf. Sci. **81**, 285 (1981).

---

[6] As a heuristic argument, as $K(\xi)$ is almost constant until its cut-off at ξ_c, we can write:
$A_H = \frac{3\hbar}{4\pi}\int_0^\infty \mathrm{d}\xi K(\xi)e^{-\alpha(\xi/c)h}$
$\sim \frac{3\hbar}{4\pi}\int_0^\infty \mathrm{d}\xi K(0)e^{-\xi/\xi_c}e^{-\alpha(\xi/c)h}$
$\sim \frac{3\hbar}{4\pi}K(0)\int_0^\infty \mathrm{d}\xi e^{-\xi(1/\xi_c+\alpha h/c)}$,
since the integral is essentially determined by the cut-off frequency imposed by α (see Fig. 5b) and therefore K can be considered as constant in the integral. Now, if $h=0$, we have: $A_{H,0} = \frac{3\hbar}{4\pi}\int_0^\infty \mathrm{d}\xi K(\xi)e^{-\xi/\xi_c} \sim \frac{3\hbar}{4\pi}\xi_c K(0)$. As a result: $A_H = \frac{3\hbar}{4\pi}\xi_c K(0)/(1+\alpha\xi_c h/c) = A_{H,0}/(1+\alpha\xi_c h/c)$.

[28] A. Checco, B. M. Ocko, A. Rahman, C. T. Black, M. Tasinkevych, A. Giacomello, and S. Dietrich, Phys. Rev. Lett. **112**, 216101 (2014).
[29] A. Checco, A. Rahman, C. T. Black, Adv. Mater. **26**, 886 (2014).
[30] J. Bico, C. Marzolin, D. Quéré, Europhys. Lett. **47**, 220 (1999).
[31] C. Cuvelier, A. Segal, and A. A. van Steenhoven, *Finite Element Methods and Navier-Stokes Equations*, Springer Science & Business Media, 1986.
[32] K. L. Mittal, *Advances in Contact Angle, Wettability and Adhesion*, John Wiley & Sons, 2013.
[33] X. Yao, Y. Hu, A. Grinthal, T.-S. Wong, L. Mahadevan, J. Aizenberg, Nat. Mater. **12**, 529 (2013).
[34] S. Srinivasan, G. H. McKinley, R. E. Cohen, Langmuir **27**, 13582 (2011).
[35] C. W. Extrand, J. Adhes. Sci. Technol. **29**, 2515 (2015).

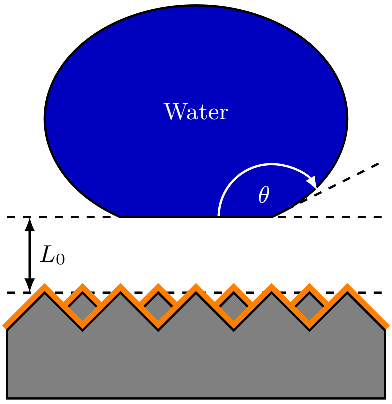
Water
θ
L_0

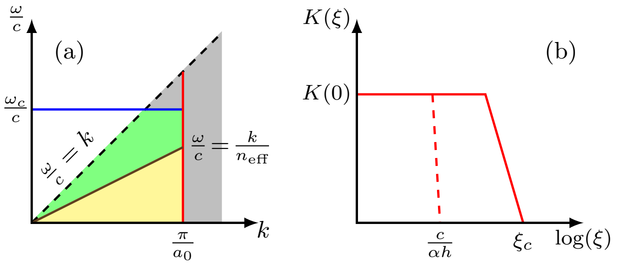
$\frac{\omega}{c}$
(a)
$\frac{\omega_c}{c}$
$\frac{\omega}{c} = k$
$\frac{\omega}{c} = \frac{k}{n_{\mathrm{eff}}}$
k
$\frac{\pi}{a_0}$
$K(\xi)$
(b)
$K(0)$
$\frac{c}{\alpha h}$
ξ_c
$\log(\xi)$

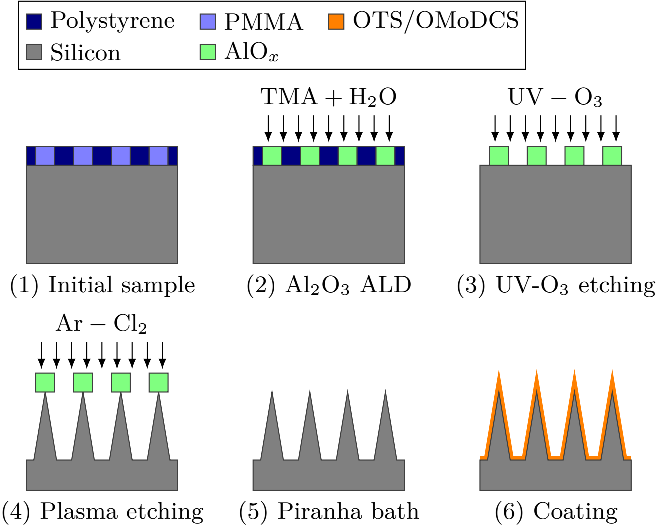

(1) Initial sample (2) Al_2O_3 ALD (3) $UV\text{-}O_3$ etching

(4) Plasma etching (5) Piranha bath (6) Coating

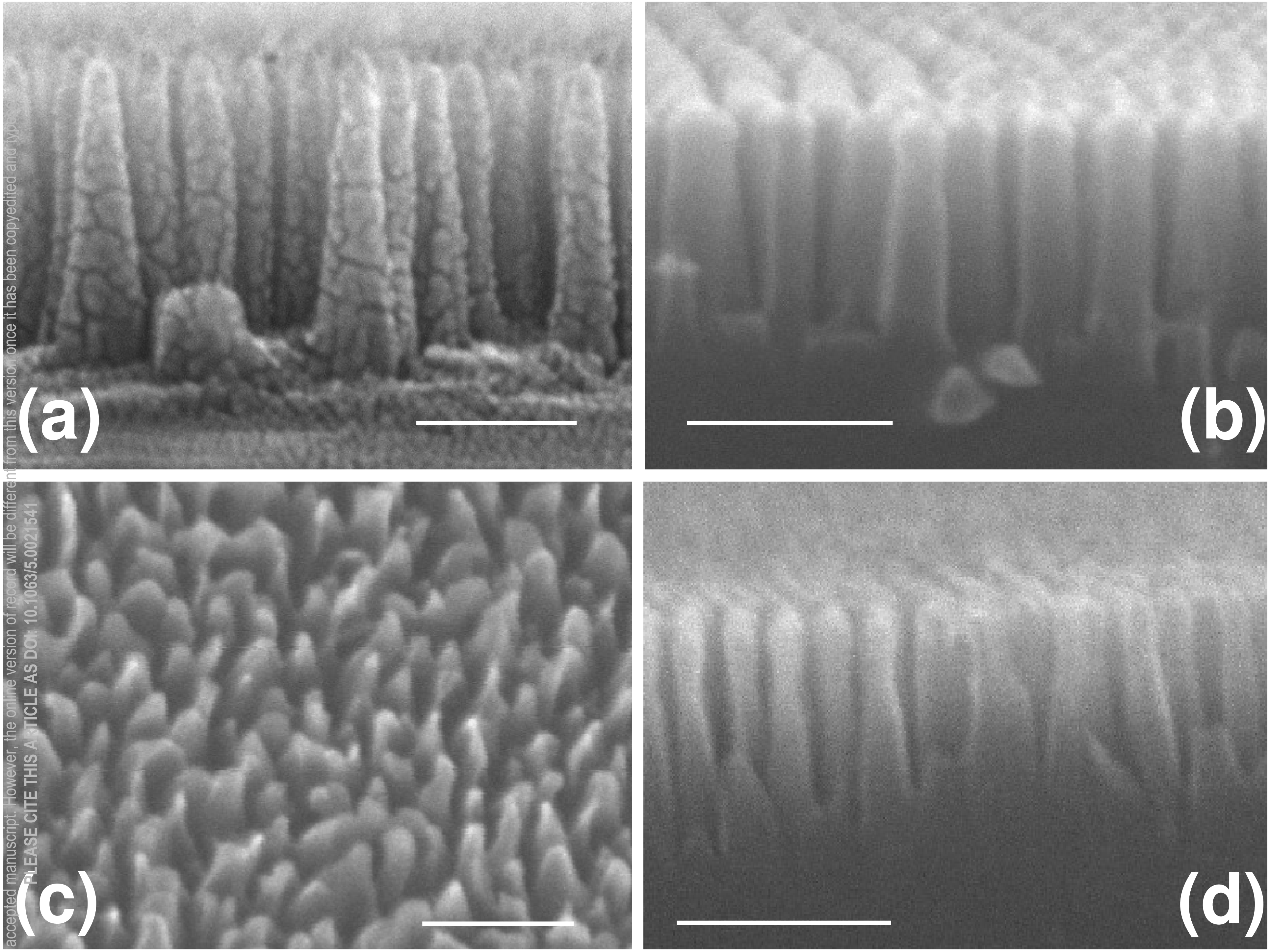
(a)
(b)
(c)
(d)

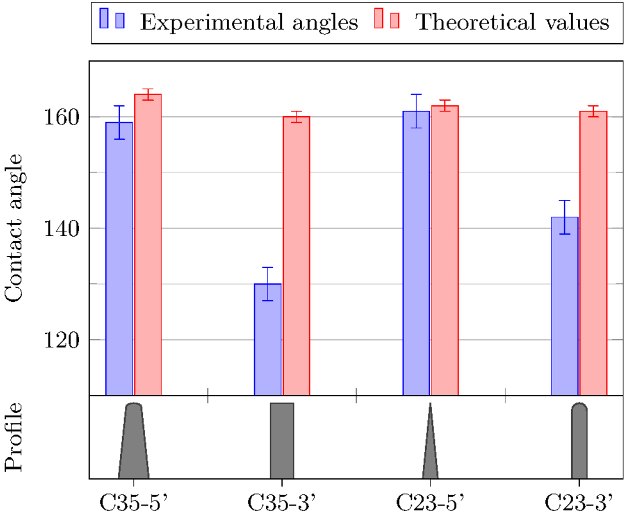
Experimental angles
Theoretical values
Contact angle
160
140
120
Profile
C35-5'
C35-3'
C23-5'
C23-3'